Polychiral Semiconducting Carbon Nanotube-Fullerene Solar Cells

Supporting Information

Authors: Maogang Gong[1]†, Tejas A. Shastry[2]†, Yu Xie[1], Marco Bernardi[4], Daniel Jasion[1], Kyle A. Luck[2], Tobin J. Marks[2,3], Jeffrey C. Grossman[4], Shenqiang Ren[1]*, and Mark C. Hersam[2,3]*

[1]Department of Chemistry, University of Kansas, Lawrence, KS 66045, United States.

[2]Department of Materials Science and Engineering, Northwestern University, Evanston, IL 60208, United States.

[3]Department of Chemistry, Northwestern University, Evanston, IL 60208, United States.

[4]Department of Materials Science and Engineering, Massachusetts Institute of Technology, Cambridge, MA 02139, United States.

*Correspondence to: shenqiang@ku.edu; m-hersam@northwestern.edu

†These authors contributed equally to this work

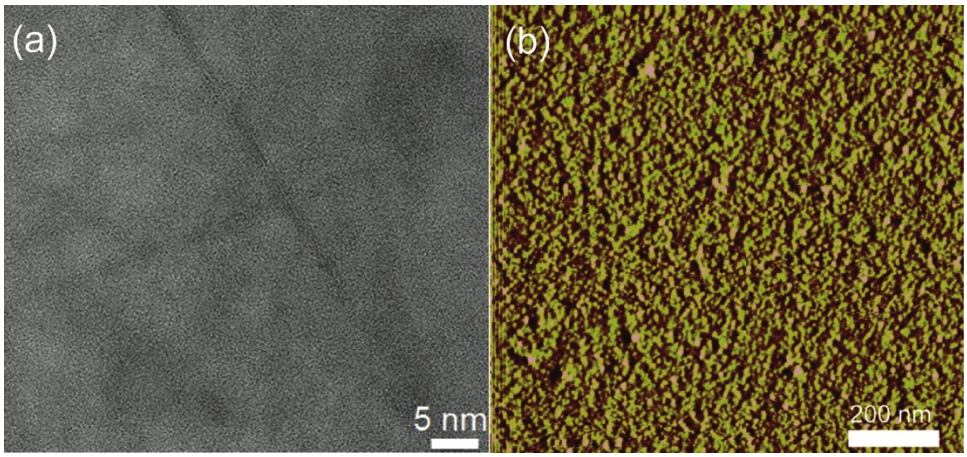

Figure S1. (a) TEM micrograph of a SWCNT wrapped with P3HT. (b) AFM micrograph of the morphology of the s-SWCNT/$PC_{71}BM$ active layer of a regular geometry cell.

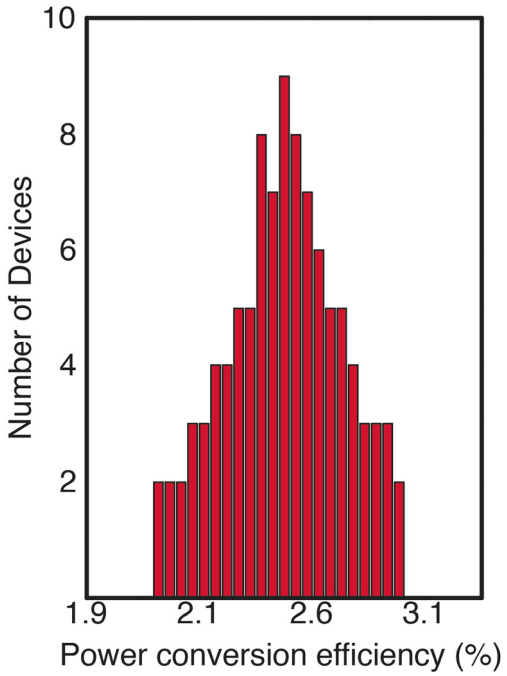

Figure S2. Histogram of 100 inverted geometry devices with an average PCE of 2.5%, a standard deviation of 0.1%, and a maximum PCE of 3.1%.

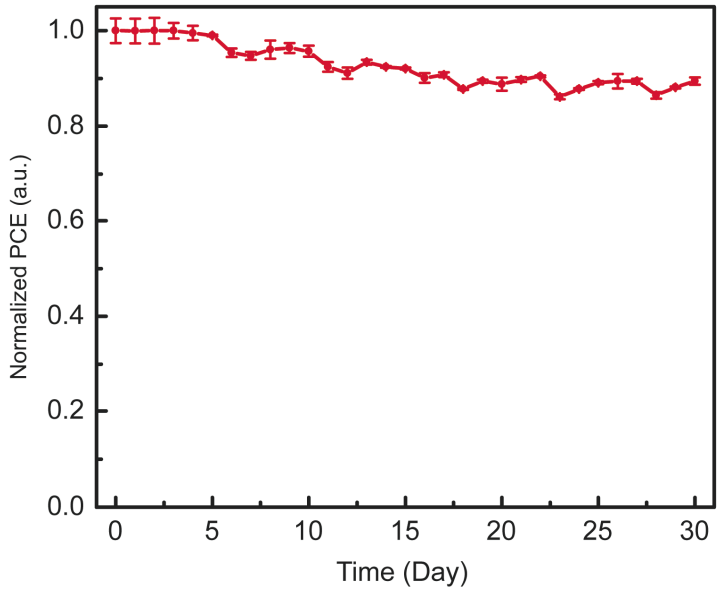

Figure S3. Degradation testing of an unencapsulated inverted s-SWCNT/$PC_{71}BM$ solar cell with 3.0% efficiency under ambient conditions.

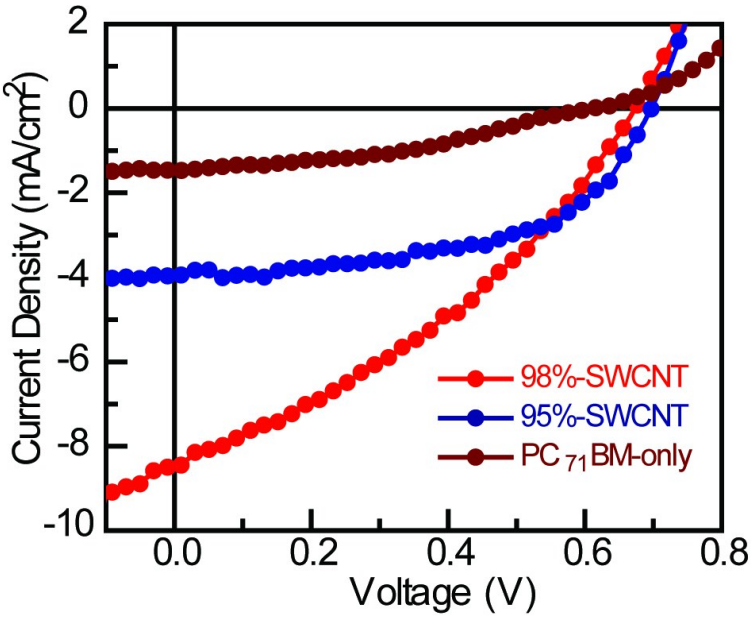

Figure S4. Illuminated *J-V* curves of regular geometry cells prepared from different semiconducting purities of s-SWCNTs and a regular geometry cell from $PC_{71}BM$ alone. Note that the $PC_{71}BM$-only cell is also in contact with the TFB spin-coated on PEDOT:PSS as shown in Figure 2a of the main text, thus including possible donor effects of the s-SWCNT dispersant polymer.

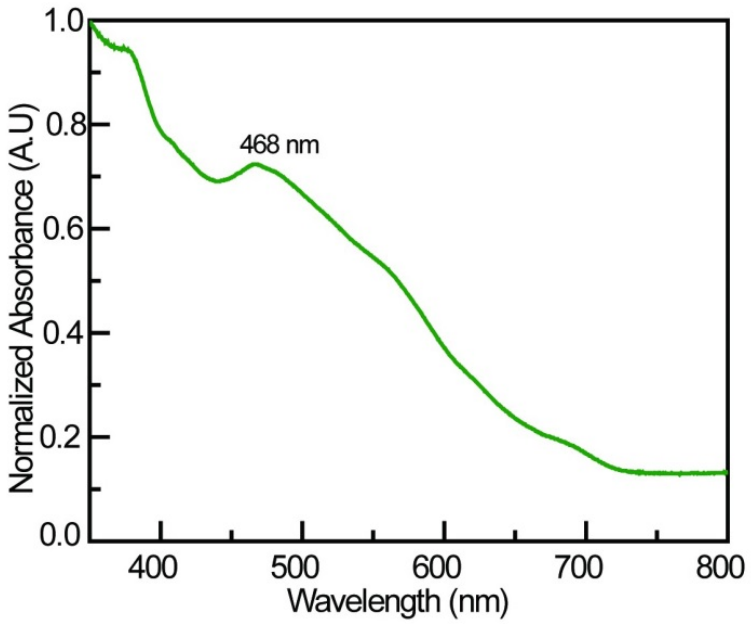

Figure S5. Normalized optical absorbance spectrum of a $PC_{71}BM$ solid film.

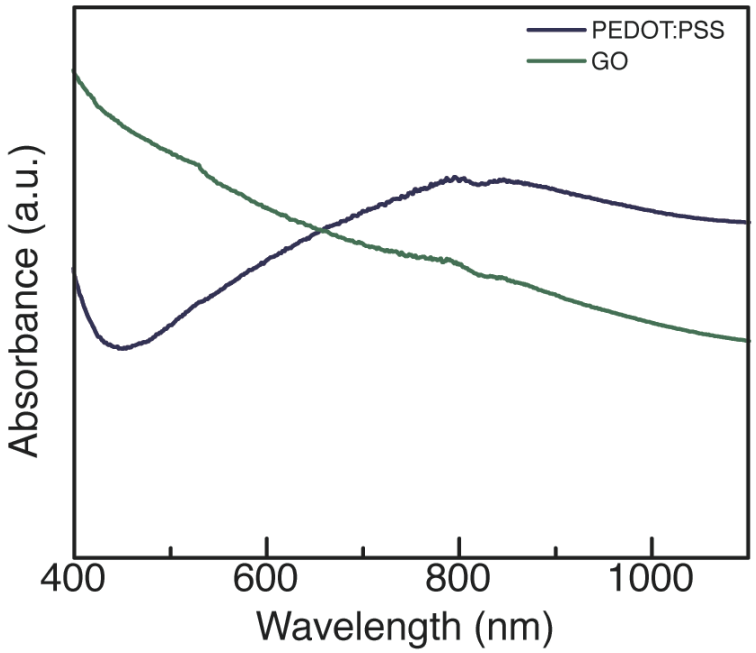

Figure S6. Optical absorbance profile of PEDOT:PSS and GO films, where GO shows high absorbance in the visible while PEDOT:PSS shows high absorbance in the near infrared.

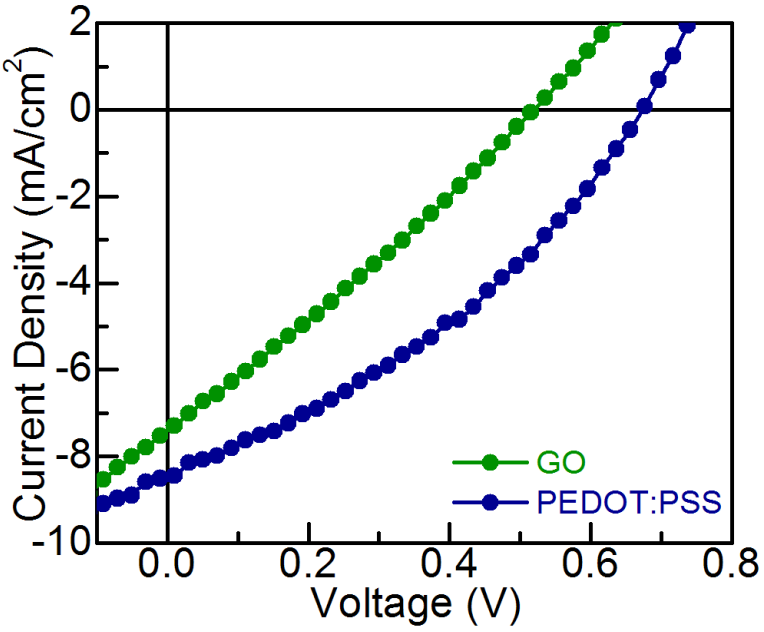

Figure S7. Illuminated *J-V* curves for s-SWCNT/$PC_{71}BM$ solar cells with PEDOT:PSS and GO interfacial layers. The cells have similar corrected currents but different voltages.

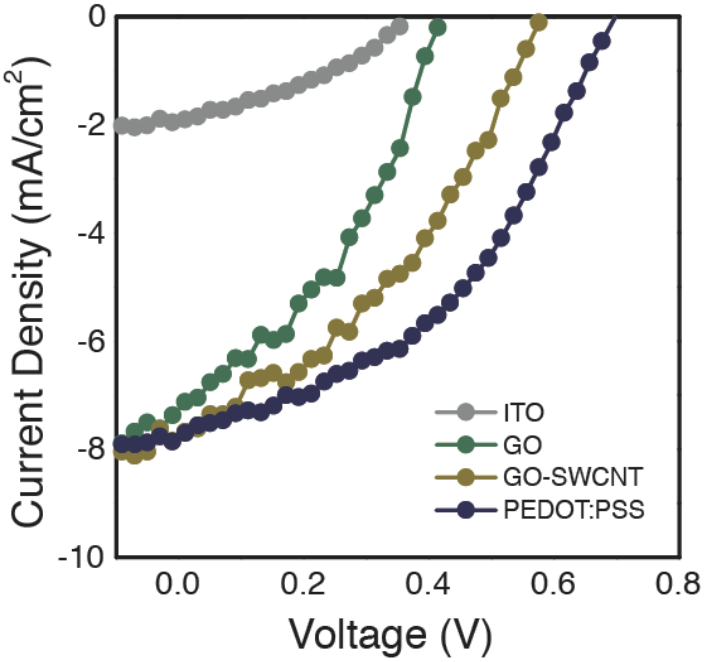

Figure S8. Illuminated *J-V* curves of cells prepared with various hole-transport layers.

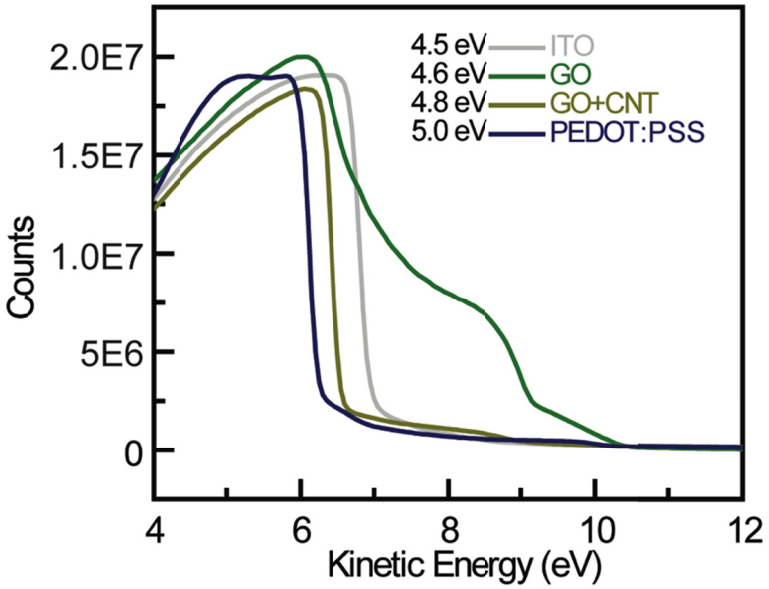

Figure S9. Ultraviolet photoelectron spectroscopy measurements of the indicated hole-transport layers prepared under conditions identical to those used in the photovoltaic cells. The broad feature extending past 7 eV for the GO sample is attributed to adsorbates on the sample that were not annealed off in order to imitate the processing conditions utilized in the fabrication of the photovoltaic cells.

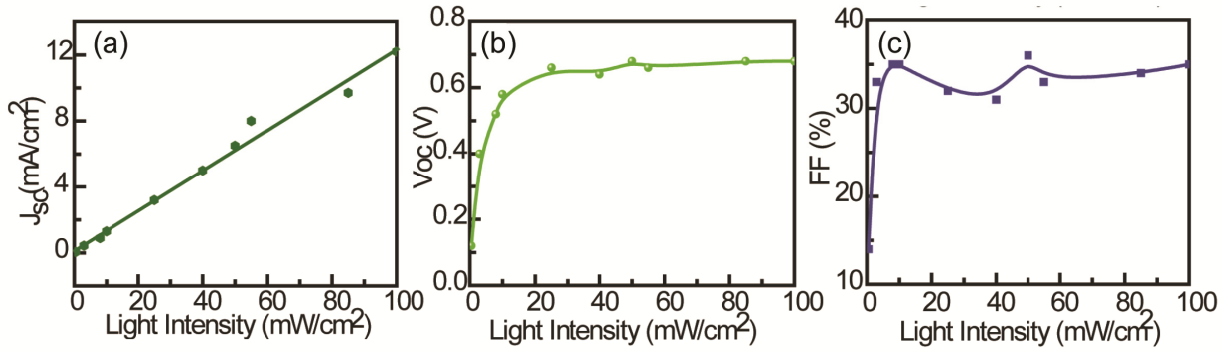

Figure S10. Light intensity dependence of (a) short circuit current density, (b) open circuit voltage, and (c) fill factor.

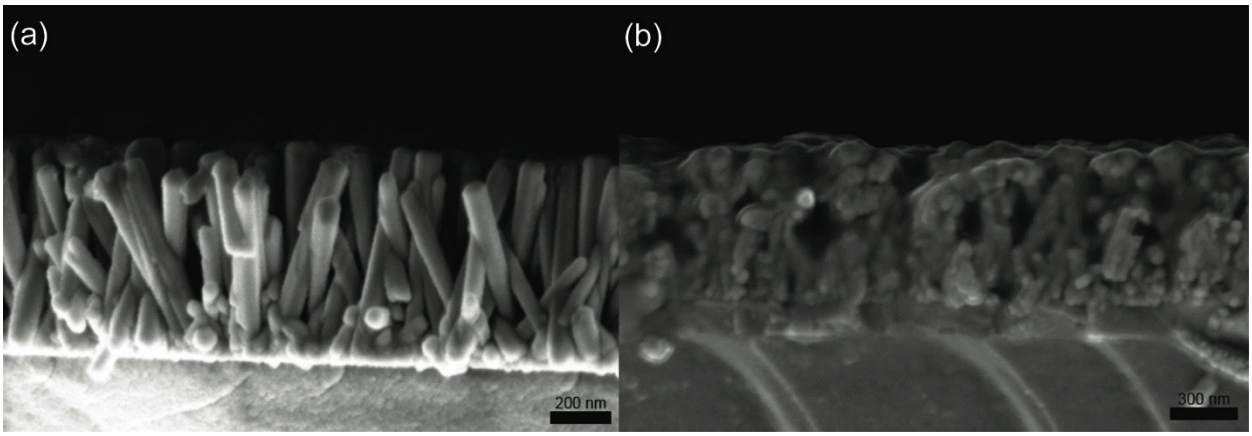

Figure S11. Cross-sectional scanning electron micrographs of (a) ZnO nanowires on ITO and (b) s-SWCNT/$PC_{71}BM$ active layer penetrated by the ZnO nanowires.

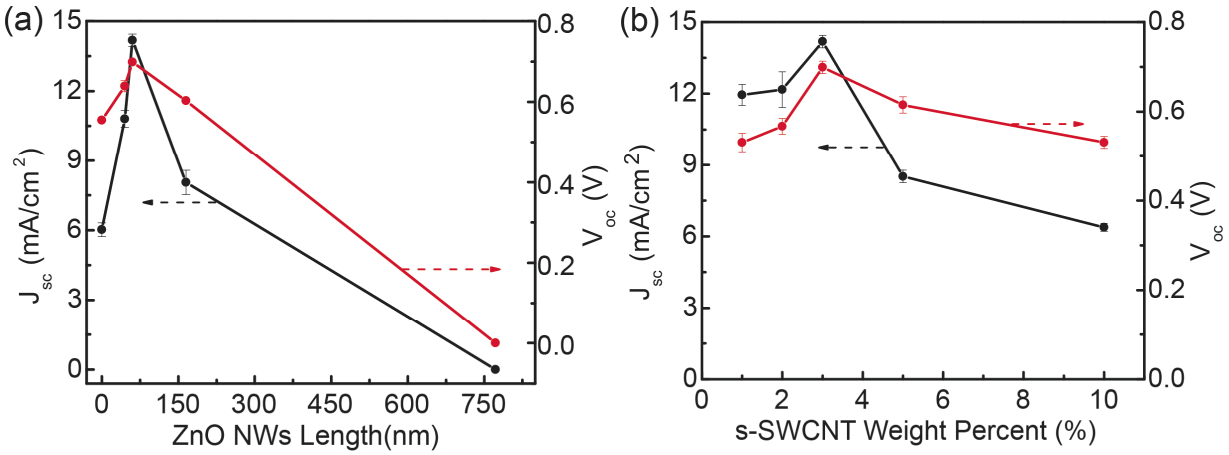

Figure S12. Optimization of (a) ZnO nanowire length and (b) s-SWCNT loading to maximize current and voltage in inverted s-SWCNT/$PC_{71}BM$ solar cells.

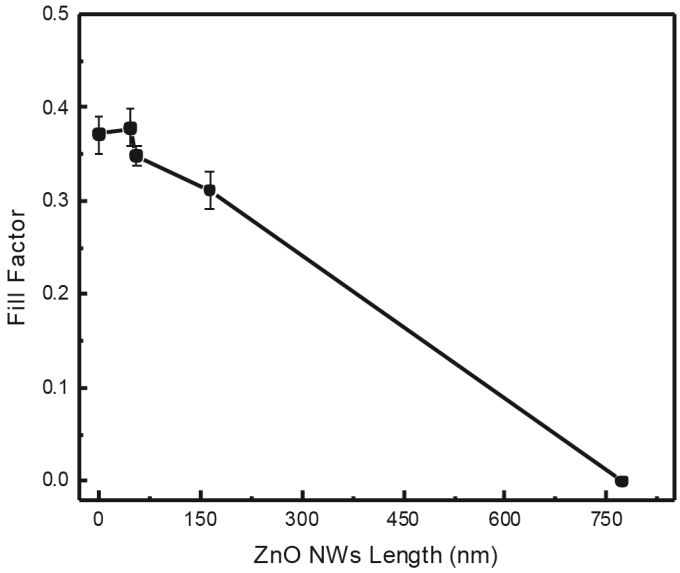

Figure S13. Dependence of fill factor (FF) on ZnO nanowire length for inverted SWCNT-fullerene solar cells.

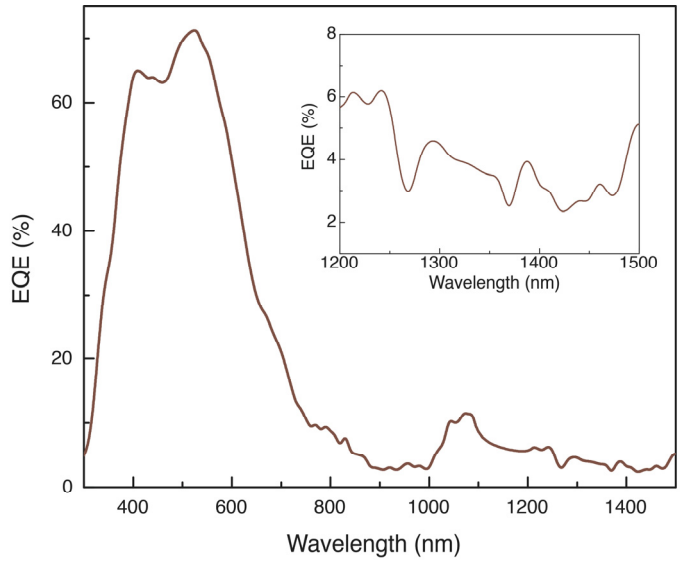

Figure S14. External quantum efficiency (EQE) of an inverted s-SWCNT/$PC_{71}BM$ cell, showing over 20% of the current resulting from NIR absorbing SWCNT transitions. A silicon detector was used from 350 nm to 1100 nm, and a germanium detector was used for longer wavelengths. A slight deviation from the common Lorentzian lineshape can be observed at 1100 nm due to the detector change.

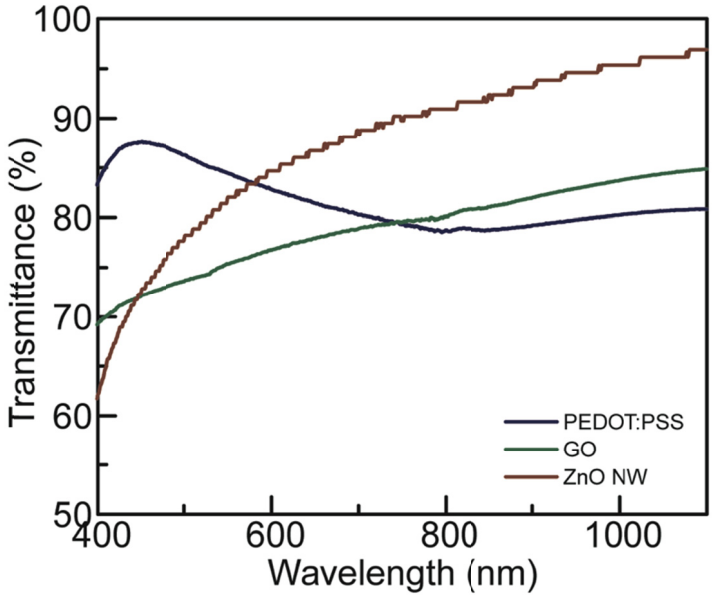

Figure S15. Transparency of PEDOT:PSS, graphene oxide, and ZnO nanowire interfacial layers throughout the visible and near-infrared regions.

Table S1. Characterization of the Chiral Distribution of HiPCo s-SWCNTs

Chirality (n,m)	S_{11} (nm)	E_{11} (eV)	S_{22} (nm)	E_{22} (eV)	Diameter (nm)
(6,4)	876	1.4	587	2.1	0.7
(8,3)	952	1.3	655	1.9	0.8
(6,5)	983	1.3	569	2.2	0.8
(8,4)	1108	1.1	587	2.1	0.8
(7,5)	995	1.2	643	1.9	0.8
(11,1)	1272	1	610	2	0.9
(10,3)	1256	1	643	2	0.9
(7,6)	1126	1.1	643	1.9	0.9
(9,4)	1108	1.1	720	1.7	0.9
(10,2)	1058	1.2	736	1.2	0.9
(11,0)	1037	1.2	756	1.7	0.9
(9,5)	1246	1	678	1.8	1
(8,6)	1177	1.1	720	1.7	1
(8,7)	1272	1	720	1.7	1
(10,5)	1256	1	798	1.6	1
(11,3)	1200	1	798	1.6	1
(12,1)	1177	1.1	798	1.6	1
(10,6)	1377	0.9	756	1.6	1.1
(9,7)	1328	0.9	798	1.6	1.1
(12,4)	1342	0.9	860	1.5	1.1
(11,6)	1397	0.9	860	1.4	1.2

Table S2. Performance of s-SWCNT/$PC_{71}BM$ Solar Cells with a Maximum PCE of 2.5%

Device #	**V_{oc} (V)**	**J_{sc} (mA/cm^2)**	**FF (%)**	**η (%)**
1	0.68	6.9	44	2.1
2	0.69	7.3	41	2.1
3	0.63	9.6	34	2.1
4	0.71	8.2	37	2.1
5	0.71	8.8	36	2.3
6	0.63	10.1	35	2.2
7	0.70	5.8	56	2.3
8	0.69	7.5	48	2.5
9	0.68	7.7	48	2.5
10	0.70	8.7	41	2.5
Average	0.68	8.1	42	2.3
Standard Deviation	0.03	1.3	7	0.2

Table S3. Performance Summary of High Efficiency Regular and Inverted s-SWCNT/$PC_{71}BM$ Solar Cells

Device Geometry	**V_{oc} (V)**	**J_{sc} (mA/cm^2)**	**FF (%)**	**η (%)**
Regular	0.68	7.8	48	2.5
Inverted	0.71	12.3	35	3.1

Table S4. Performance Summary of Various Semiconducting Purity s-SWCNT/$PC_{71}BM$ Solar Cells and a Pure $PC_{71}BM$ Solar Cell

Material	**V_{oc} (V)**	**J_{sc} (mA/cm^2)**	**FF (%)**	**η (%)**
98% s-SWCNT	0.68	8.5	36	2.1
95% s-SWCNT	0.70	4.0	55	1.5
Pure $PC_{71}BM$	0.60	1.5	39	0.35

Table S5. Measured Performance Summary of 98% Purity s-SWCNT/$PC_{71}BM$ Solar Cells with Different Interfacial Materials or Bare ITO

Interface Material	**V_{oc} (V)**	**J_{sc} (mA/cm^2)**	**FF (%)**	**η (%)**
PEDOT:PSS	0.68	8.1	35	1.9
GO-SWCNT	0.60	7.9	37	1.8
GO	0.52	7.8	27	1.1
ITO	0.37	1.9	35	0.25